Synthesis and characterization of PANI-CZF nanocomposites for enhanced electromagnetic interference shielding

G. Harisha[1,2], D. R. Rangaswamy[3], R. Thejas[4], C. Devaraja[5,]*[ID], M. Revanasiddappa[6], M. V. Murugendrappa[7], and K. M. Rajashekara[1,]*

[1] *Department of Physics, S J C Institute of Technology, Chickballapur, Karnataka 562101, India*

[2] *Visvesvaraya Technological University, Belagavi, Karnataka 590018, India*

[3] *Department of Physics, PES University–Electronic City Campus, Bangalore, Karnataka 560100, India*

[4] *Department of Physics, Presidency University, Bengaluru, Karnataka 560064, India*

[5] *Department of Physics, Manipal Institute of Technology Bengaluru, Manipal Academy of Higher Education, Manipal, Karnataka 576104, India*

[6] *Department of Chemistry, PES University–Electronic City Campus, Bengaluru, Karnataka 560100, India*

[7] *Department of Physics, B.M.S. College of Engineering, Bengaluru, Karnataka 560019, India*

ABSTRACT

The $Zn_{0.5}Cu_{0.5}Fe_2O_4$ nano ferrites were prepared by the solution combustion method using aloe vera gel. The polyaniline-$Zn_{0.5}Cu_{0.5}Fe_2O_4$ nano ferrite composites were prepared by Ex-situ polymerization method with different weight percentage ratio. The prepared samples were examined by X-Ray diffraction, SEM, EDAX, BET, TEM, VSM and Impedance analyser to investigate their structural, morphological, elemental analysis, average pore size and the porosity, magnetic, and dielectric properties, respectively. The cubic spinel structure was confirmed by X-ray diffraction patterns. Addition of PANI to zinc-copper nano ferrite exhibits shift in crystalline peaks towards larger angle. The existence of spherical and clumped particles was revealed by SEM examination. The retentivity and coercivity are determined and the magnetic moment values were decreases with increase in PANI to the ferrite nanocomposites. The ac conductivity constant at lower frequency and there is a sudden increase and decrease in its value as a function of frequency shows resonance behaviour. The CZF-1 (CZF 30%) composite shows highest ac conductivity and dielectric constant. The electromagnetic shielding interference studies were conducted for S-band frequency. The CZF-1 (CZF 30%) nano composite shows highest shielding effectiveness as compared to other composite in the frequency range 2 to 3 GHz. The experimental result showed that these materials are used for applications in electromagnetic interference shielding.

Address correspondence to E-mail: devaraja.c@manipal.com; km_rajashekar@yahoo.co.in

🍀 Springer

1 Introduction

There has been a huge growth in demand for the production of absorbing materials to reduce the effect of electromagnetic radiation interference (EMI) [1]. EMI and its impact on electronic devices have been ongoing for decades. In recent years, there has been an increased focus on the impact of EMI on medical devices [1, 2], such as implantable devices and pacemakers. Additionally, there has been a growing interest in the effect of EMI on autonomous vehicles and their sensors [2]. To obtain high-quality microwave absorbing properties, it is necessary for shielding materials to exhibit two fundamental characteristics: wave attenuation, which refers to the ability to reduce the amplitude of electromagnetic waves as they pass through the material layer, and impedance matching [3], where the resistance of the material should be equivalent to that of free space to minimize wave reflection [4]. Alongside these essential attributes, other factors such as low weight, thinness, high mechanical strength, miniaturization, wide absorption-reflection loss, and resistance to environmental factors should also be considered when producing and designing microwave absorbing materials [5]. Although they are bulky and costly, ferrite absorbers have been produced throughout the years to research the microwave absorbing capabilities. It has been discovered that they display outstanding magnetic and dielectric qualities [5]. Ferrite nano composites have attracted tremendous interest in various fields such as biomedicine, sensing, energy storage, satellite communication, mobile communication, and environmental applications due to their unique properties, including high surface area, biocompatibility, and magnetic behaviour [6]. Among these magnetic nanoparticles, Copper–Zinc ferrites have been widely studied because of their high magnetic moment, excellent stability, and potential applications in various areas. Similarly, researchers have shown that a variety of plant extracts are used in the production of nanoparticles with diameters ranging from 5 to 50 nm [6, 7]. But aloe vera is recognised as a boon among them due to its availability in large quantities in Indian lands and other countries. The 99.5% of water content and 1.5% of water along with 75 different ingredients made aloe vera as unique material for green synthesis. In addition, it is employed in "pharmacology" for the treatment of "burns and inflammation" [7]. The particle size is varied to nanometers using aloe vera,

which is an excellent reducing agent [8, 9]. Polymers have been recognized as an attractive material for numerous applications, including energy storage, electrochromic devices, and biosensors [10]. Polymers, especially conductive polymers, have been widely researched in the field of electromagnetic interference (EMI) shielding. Among these, polyaniline (PANI) has shown great potential for EMI shielding applications due to its excellent electrical conductivity, low density, and ease of synthesis. The result shows that $ZnFe_2O_4$/Polyaniline/Graphene oxide composite has excellent absorbing property [10]. M A Almessiere et.al study explores the impact of manganese and yttrium co-substitution on the morphology and magnetic properties of strontium nano hexaferrites [11]. Slimani, et al. are reported the electrical and dielectric characteristics of ceramics made of $BaTiO_3$ and $SrTiO_3$ are significantly influenced by the study of WO_3 nanoparticles. This study probably explores the modifications and improvements introduced into the ceramic composition at the nanoscale by the presence of WO_3 [12]. A Safeen et.al studied the explorations of the influence of dual doping with manganese (M_n) and cobalt (C_o) on ZnO nanostructures and reported the how this process affects their structural, optical, dielectric, and magnetic properties [13]. Jabbar et al. shows the properties of ZnO nanoparticles doped with transition metal elements, providing an in-depth look into the properties of diluted magnetic semiconductors [14]. Izaak et al. explored the various properties of $ZnFe_2O_4$, such as its magnetic, electrical properties, and how they contribute to its absorption capabilities [15]. Zulfiqar et.al, examined the impact of oxygen vacancies on room temperature ferromagnetism and improved dielectric properties in ZnO nanoparticles co-doped with cobalt (Co) and manganese (M_n) [15]. Khan et al. studied the effects of doping ZnO nanoparticles with tin (Sn) on their structural, optical, dielectric, and magnetic characteristics, with an emphasis on the possible uses of this information in spintronics [16]. Naagar et al. showed the various properties of nano ferrites, including their electrical and magnetic properties, and how they can be utilized to enhance the performance of randoms [16]. Khan et al. investigated the effects of oxygen vacancies on the structural, dielectric, and magnetic characteristics of ZnO nanostructures co-doped with cobalt (Co) and manganese (M_n) follow [17]. Khan et al. work focuses on the magnetic properties and structure of ZnO-based nanoparticles co-doped with cerium (Ce) and cobalt (Co).

It investigates the addition of these components and how it affects the material's diluted magnetic semiconductor characteristics [18]. In particular, the magnetic behaviour arising from the (Co, Ce) co-doping in ZnO nanoparticles is investigated, and the structural features are explored. Madhu et al. discussed the properties of polyaniline/ferrite composites, including their structural, dielectric, AC conductivity, and electromagnetic shielding properties [19]. Salem et al. noted YBa_2Cu_3O microstructure and pinning qualities are significantly altered by the addition of SiO_2 nanoparticles [19]. The superconducting properties of polycrystalline $YBa_2Cu_3O_7$–d, formed through the sintering process of ball-milled precursor powder, are investigated, and reported [20]. To the best of our knowledge, there hasn't been any documentation on the synthesis of nanocomposites of $Cu_{0.5}Zn_{0.5}Fe_2O_4$ using the solution combustion method with aloe vera as fuel, with purposefully varied polyaniline compositions by ex-suit technique, despite the difficulties of meeting the combined demands for thinness, lightness, reflection loss, and absorption properties required for creating EMI shields. The aim of the present investigation is to synthesis $Cu_{0.5}Zn_{0.5}Fe_2O_4$ nano powders by employing solution combustion as a green synthesis technique. Additionally, using the ex-suit approach, $Cu_{0.5}Zn_{0.5}Fe_2O_4$ and Polyaniline (PANI) nanocomposites with systematically different compositions were produced. Due to its saturation magnetization and dielectric constant, $Cu_{0.5}Zn_{0.5}Fe_2O_4$ was selected. The $Cu_{0.5}Zn_{0.5}Fe_2O_4$/PANI composite's complex permittivity, conductivity fluctuation, magnetic property and reflection loss were studied for various thicknesses. The use of spinel ferrites in these investigations is consistent with the larger framework of developing materials for a variety of uses, from superconductivity to EMI shielding, illustrating their potential influence on a range of technological frontiers.

2 Materials and methods

2.1 Materials used

AR grade zinc nitrate [$Zn (NO_3)_2 6H_2O$], copper nitrate [$Cu(NO_3)_2.6H_2O$], ferric nitrate [$Fe(NO_3)_3 9H_2O$], Aniline, Ammonium persulphate (APS), Hydrochloric acid (1N), ethanol, aloe vera, and distilled water were used as starting raw materials.
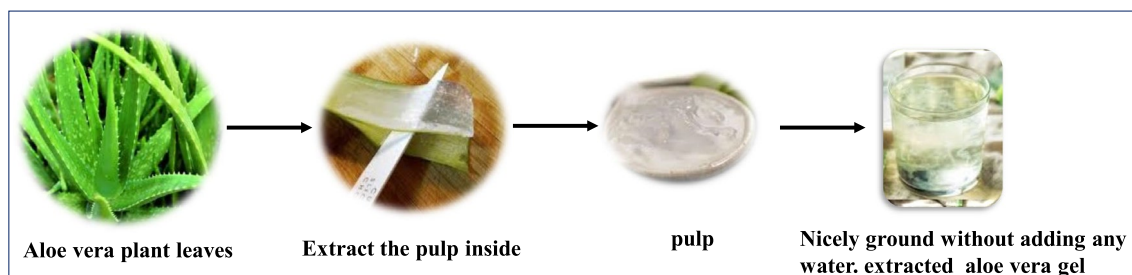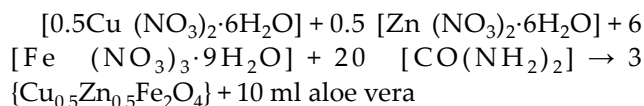
2.2 Preparation of aloe vera gel

Aloe barbadensis miller is the scientific name of aloe vera, and it is a member of the *Liliaceae* (*Asphodelacease*) family. The pulp inside the aloe vera leaves is released by gently picking them up, cleaning them properly, and scraping them. Without using any water, the pulp is next thoroughly crushed. Then this is filtered through purified muslin fabric to remove the precipitate. The procedure of solution combustion is then carried out using this precipitate. The Fig. 1 shows the preparation of aloe vera gel.

2.3 Synthesis of $Zn_{0.5}Cu_{0.5}Fe_2O_4$

The preparation of ferrite through the outlined steps involves the meticulous transformation of metal nitrates into metal oxides using a combustion reaction induced by aloe vera as a fuel. The subsequent oxide formation during combustion is followed by a crucial calcination process, where controlled heating facilitates crystallization and phase formation, ultimately resulting in the desired nano ferrite structure.

Chemical reaction

[$0.5Cu (NO_3)_2 \cdot 6H_2O$] + 0.5 [$Zn (NO_3)_2 \cdot 6H_2O$] + 6 [$Fe (NO_3)_3 \cdot 9H_2O$] + 20 [$CO(NH_2)_2$] → 3 {$Cu_{0.5}Zn_{0.5}Fe_2O_4$} + 10 ml aloe vera

| Aloe vera plant leaves | Extract the pulp inside | pulp | Nicely ground without adding any water. extracted aloe vera gel |

Fig. 1 Schematic representation of aloe vera gel preparation

Analytical pure Zn $(NO_3)_2 \cdot 6H_2O$, Cu $(NO_3)_2 \cdot 3H_2O$, and Fe $(NO_3)_3 \cdot 9H_2O$ (< 98% AR grade metal nitrates) were used as starting materials. These materials were combined in the appropriate stoichiometric ratio along with 20 ml of Aloe vera solution (C16H13NO3) to create ferrite. ("Acemannan" and "aloin" are the main active ingredients in aloe vera gel; acemannan's chemical formula is $C_{19}H_{28}O_{14}$, whereas aloe vera's molecular formula is $C_{16}H_{13}NO_3$). The 50 ml of deionized water was added to resulting mixture with constant stirring for 45 min. Then, the mixture was ultrasonicated around 20 min to create homogeneous solution. The solution was heated up to 450 °C. $Zn_{0.5}Cu_{0.5}Fe_2O_4$ nano ferrites are effectively synthesised by the solution combustion process. This approach, which was chosen for its ease of use and affordability, produces finely split nanostructures with control over the size and structure of the particles, which makes it perfect for accurate $Zn_{0.5}Cu_{0.5}Fe_2O_4$ nano ferrite production, the prepared samples are termed as CZF. The obtained materials were crushed into powder by using agate mortar. The powder samples were calcinated at 800 °C up to 1 h to remove moisture and unwanted contaminants.

2.4 Synthesis of PANI

With constant stirring, 0.1 M aniline dissolved in 100 mL of 1 M HCl solution. Then kept the solution in the ice bath for 2 to 3 h by adding 0.1 M ammonium persulfate solution dropwise along the side of the beaker. The dark green solution was obtained and then centrifuged to separate the precipitate. Lastly, systematically washed the obtained precipitate with deionized water and methanol.

2.5 Synthesis of PANI-ferrite composite

For the PANI-$Zn_{0.5}Cu_{0.5}Fe_2O_4$ nanocomposite, the appropriate weight percentage of nano ferrite and PANI has been dissolved in 50 mL of ethanol as tabulated in Table 1. To achieve the homogeneity in the mixture 80 min of sonication at 35 °C have been carried out, the solution underwent filtration and extensive washing with distilled water until the washings reached pH = 7. Further, the solution is kept at room temperature for around 12 h to remove ethanol from the mixture. The composite material was washed multiple times with ethanol, and then dried.

Table 1 The different weight percentages of PANI and $Zn_{0.5}Cu_{0.5}Fe_2O_4$ in each sample of PANI/$Zn_{0.5}Cu_{0.5}Fe_2O_4$ nanocomposites

| Samples	Nomenclature	PANI wt%	CZF wt%
PANI	PANI	100	0
$Zn_{0.5}Cu_{0.5}Fe_2O_4$	CZF	0	100
$Zn_{0.5}Cu_{0.5}Fe_2O_4$/PANI	CZF1	70	30
$Zn_{0.5}Cu_{0.5}Fe_2O_4$/PANI	CZF2	60	40

3 Result and discussion

3.1 XRD

Figure 2 depicts the X-ray diffraction (XRD) spectra of PANI-CZF nanocomposites. The XRD spectrum shows pure PANI with no sharp peaks, which indicates a nanocrystalline, amorphous nature. However, a diffuse broad peak ranging from 15° to 30° was observed, which is non-crystalline. The PANI-CZF nanocomposites exhibit crystalline peaks due to the presence of ferrite in these nanocomposites. The original broad peaks of pure PANI disappeared due to the incorporation of ferrite nanocomposites. The PANI-CZF nanocomposites are in the spinel cubic structure, and the copper ferrite matches JCPDS card no. 901–2438, and zinc ferrite findings were also found to be consistent with the accepted references (JCPDS file no. 22–1012). The XRD pattern of PANI-CZF nanocomposites (Fig. 2) shows that the main characteristic peaks of CZF are consistent with the Fd^{-3} m spinel cubic structure with indexed planes near (220), (311), (400), (442), (511), and (440), respectively [20–22]. This supports the copper phase, PANI, and ferrite spinel phase's coexistence [23]. With the use of Scherrer's Eq. (1), the average crystalline size was determined.

$$D_{hkl} = \frac{0.94\lambda}{\beta\cos\theta} \tag{1}$$

where, λ = X-ray wavelength equal to 1.5406 Å, θ = Bragg diffraction angle, β (radians) = full width at half maximum.

The average crystallite size of the samples was determined from the most conspicuous XRD line width of the 311 peaks. Changes in particle size can influence peak broadening in XRD patterns. Smaller particle sizes often lead to broader peaks. If the addition of PANI influences particle size, it could contribute to the observed changes in peak shape [24], and
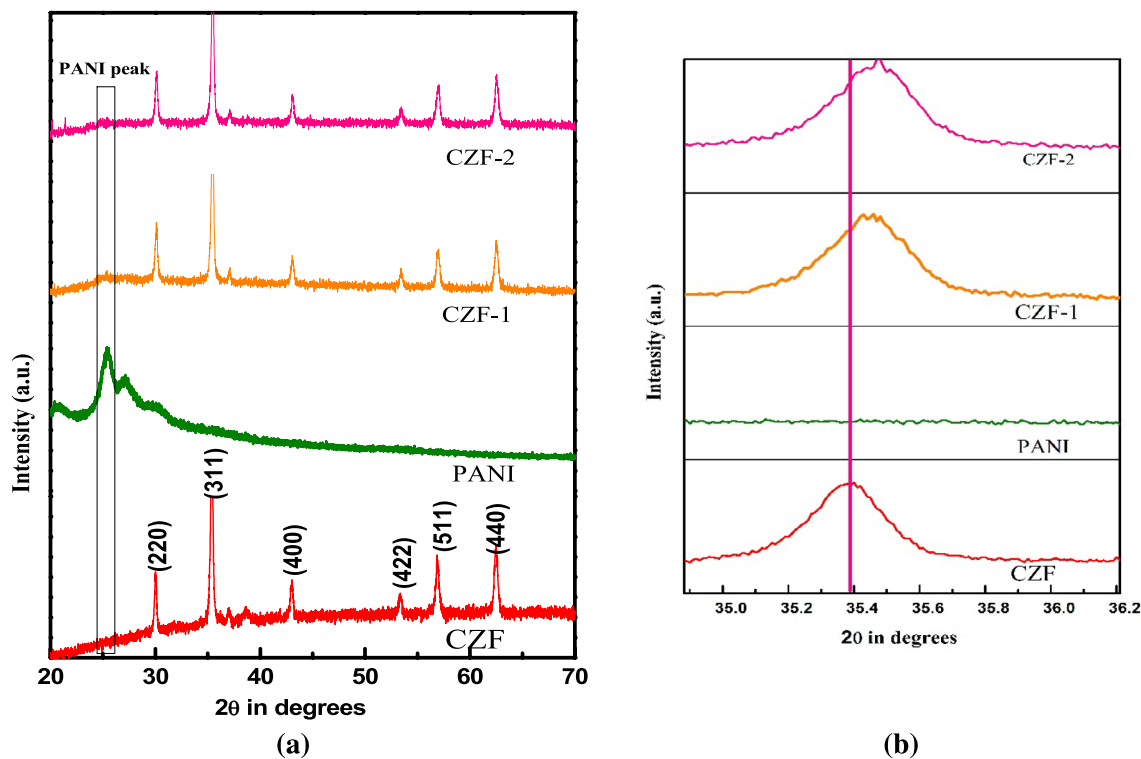
Fig. 2 a XRD peaks of CZF, PANI, CZF-1, CZF-2 nano composites. **b** XRD peaks shift at an angle 35.4° of CZF, PANI, CZF-1, CZF-2 nano composites

it was discovered that crystallite sizes typically fall between 40 and 60 nm [20, 25]. From the spectra, it was observed that there is a shift in peak position with an increase in PANI in the composite, attributed to a small modification in the structure of the nanocomposites. The lattice parameters of the composite may undergo changes due to the introduction of PANI. This alteration in the crystal lattice could result in a shift in diffraction peaks. A similar trend was observed in the several reported studies done by different researchers [26, 27].

Figure 3 illustrates the Rietveld refinement plots of CZF sample, the method is considered to do the quantitative analysis of the secondary phase along with spinal phase and obtained data is tabulated in Table 2. This refinement approach allows for the detailed understanding of the structural changes and influences on XRD patterns. Figure 4 depicts the crystal structure of CZF.

3.2 FTIR

Figure 5 illustrates the FTIR spectra of PANI, CZF, CZF1 and CZF2 nanocomposites. The C=C quinoid band (1598 cm^{-1}) of PANI was shifted towards the lower band (~ 1558 cm^{-1}) for the nanocomposites and C=C benzenoid rings are shifted from 1494 to ~ 1470 cm^{-1} [28, 29]. C–N stretching vibrations of the PANI-CZF nanocomposites were shifted to the lower band compared to pure PANI (1295 to ~ 1288 cm^{-1}). N=Q=N wide range vibrational band of PANI was found to be ~ 1119 cm^{-1} but for the PANI-CZF nanocomposites was found to be ~ 1075 cm^{-1}. The band at 776 cm^{-1} for PANI but for PANI-CZF nanocomposites was shifted towards higher band of ~ 793 cm^{-1} this was attributed due to the out of-plane deformation of C-H in the 1,4-disubstituted benzene ring [30, 31]. The PANI-CZF nanocomposites shows characteristic bands of CZF nanoparticles at ~ 554 cm^{-1}, this was due to the presence of the structural vibrations in tetragonal metal-oxide (Zn^{2+}–O^{2-}, Fe^{3+}–O^{2-}) bonds & ~ 395 cm^{-1} was due to the presence of the structural vibrations of octahedral metal-oxide (Cu^{2+}–O^{2-}, Fe^{3+}–O^{2-}) bonds [32].
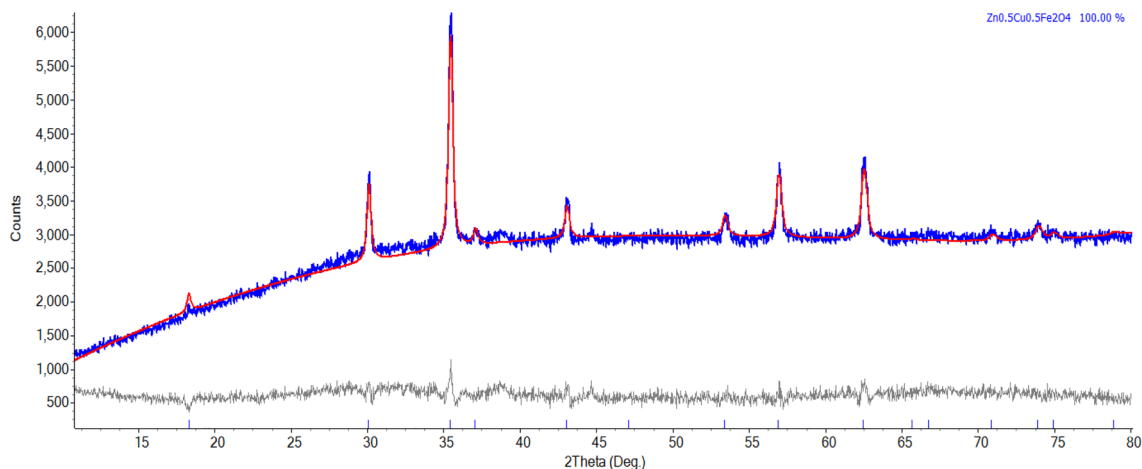
Fig. 3 Rietveld refinement plots of CZF

Table 2 Rietveld refinement parameter from the PXRD data for $Cu_xZn_{1-x}Fe_2O_4$(X = 0, 0.3, 0.5, 0.7, 1)

Compound name	Crystal system	Crystal system	Crystallite size (nm)	Parameter (A^0)		R–factors			
				a = b = c	Cell volume ($A^{0\,3}$)	R_p	R_{wp}	GOF(χ^2)	R_{exp}
CZF	Fd^{-3} m	Spinal cubic	34.94	8.40	594.43	2.18	2.78	1.45	1.92
CZF-1			6						
CZF-2			16						
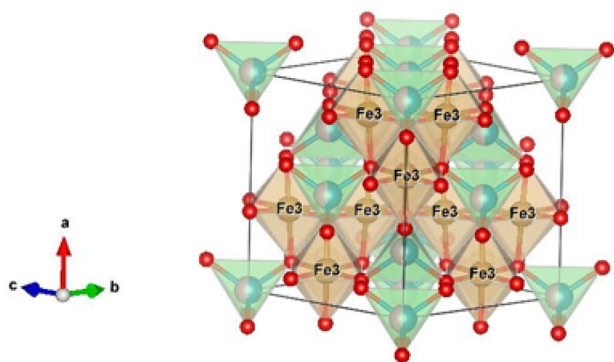
Fig. 4 CZF crystal structure

3.3 Brunauer–Emmett–Teller (BET) analysis

The N_2 Adsorption plot of synthesized samples is shown in Fig. 6a which belongs to the type II adsorption isotherm. For each of the PANI, CZF, CZF-1 samples, the absorbed amount of N_2 showed a gradual increment, for CZF-1 composite sample implying the presence of highly pore structure [33, 34]. According to Brunauer–Emmett–Teller calculations [35] the specific pore surface area of PANI,

CZF, CZF-1 samples were found to be in the range of 39.455 to 13.727 m^2g^{-1} as shown in Fig. 6b. As the crystallite size rises, the surface area was found to increase. In general, crystal size decreases for the composites and porosity increases with increase in the relative pressure of the sample.

The best explanation for this usual behaviour of polymer-metal oxide composites is the concept of nucleation and crystal development. In the case of metal oxides, the number of defects decreases with concentration, which lowers the number of atoms per unit area. The Barrett-Joyner-Halenda (BJH) technique [36] is used to determine the distribution of pore sizes as in Fig. 7a–d. The average pore diameter of PANI was found to be 1.955 nm, CZF which is 3.996 nm and the composites shows 1.929 nm. It is found to have a mesoporous structure; pore diameter increases as the specific surface area decreases. The porous structures and abundant gaps in the samples, according to Junlei Qi et al., are advantageous for achieving full contact with electrolytes and offer advantages in buffering the volume changes in long-term tests, resulting in better performance of EMI shielding materials.

Fig. 5 FTIR spectra of **a** PANI **b** CZF **c** CZF-1**d** CZF-2
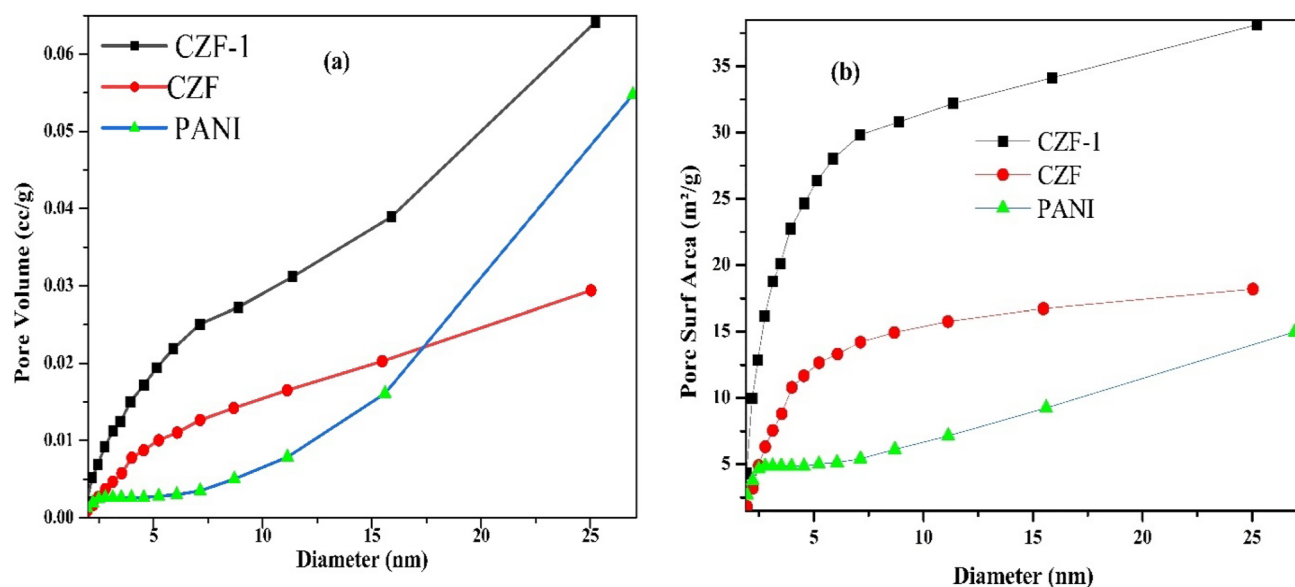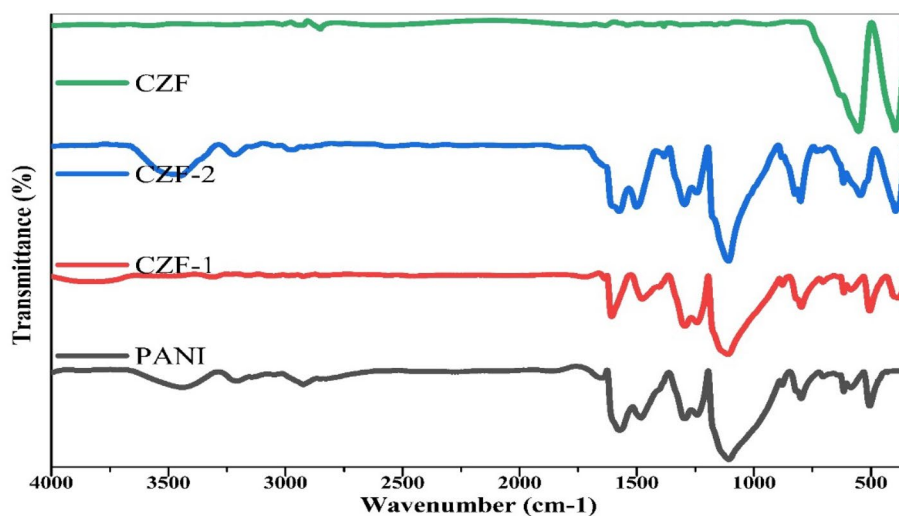

Fig. 6 BET **a** pore volume and **b** pore surface area spectra of PANI, CZF, CZF-1 sample

3.4 SEM and EDX analysis

Figure 8 shows the SEM micrographs of PANI-CZF nanocomposites. The well-granular, non-porous, and agglomerated structure with a homogeneous surface were observed, indicating that PANI layers might arranged on the surface of CZF nano composites. A closer examination of these primary structures reveals that nearly spherical particles with an average particle size of 40–60 nm. The composites were well mixed with PANI, one can observe that the ferrites samples were surrounded with PANI and no extra granules of ferrites were seen on the surface of the sample. Comparing the observed nanoparticles with the crystallite size estimated from X-ray suggests that the observed nanoparticles may have crystalline character [37–39].

The analysis tool known as energy-dispersive X-ray (EDX) spectroscopy is used to ascertain the chemical make-up of a material. Energy-dispersive X-ray (EDX) analysis is used to verify the elemental assessment in the instance of PANI/CZF nano ferrites [40]. The findings are displayed in Fig. 9. Iron (Fe), zinc (Zn), copper (Cu), oxygen (O), nitrogen (N), carbon (C), and chlorine (Cl) are detected in the prepared samples of (a) PANI, (b) CZF, (c) CZF-1, and (d) CZF-2
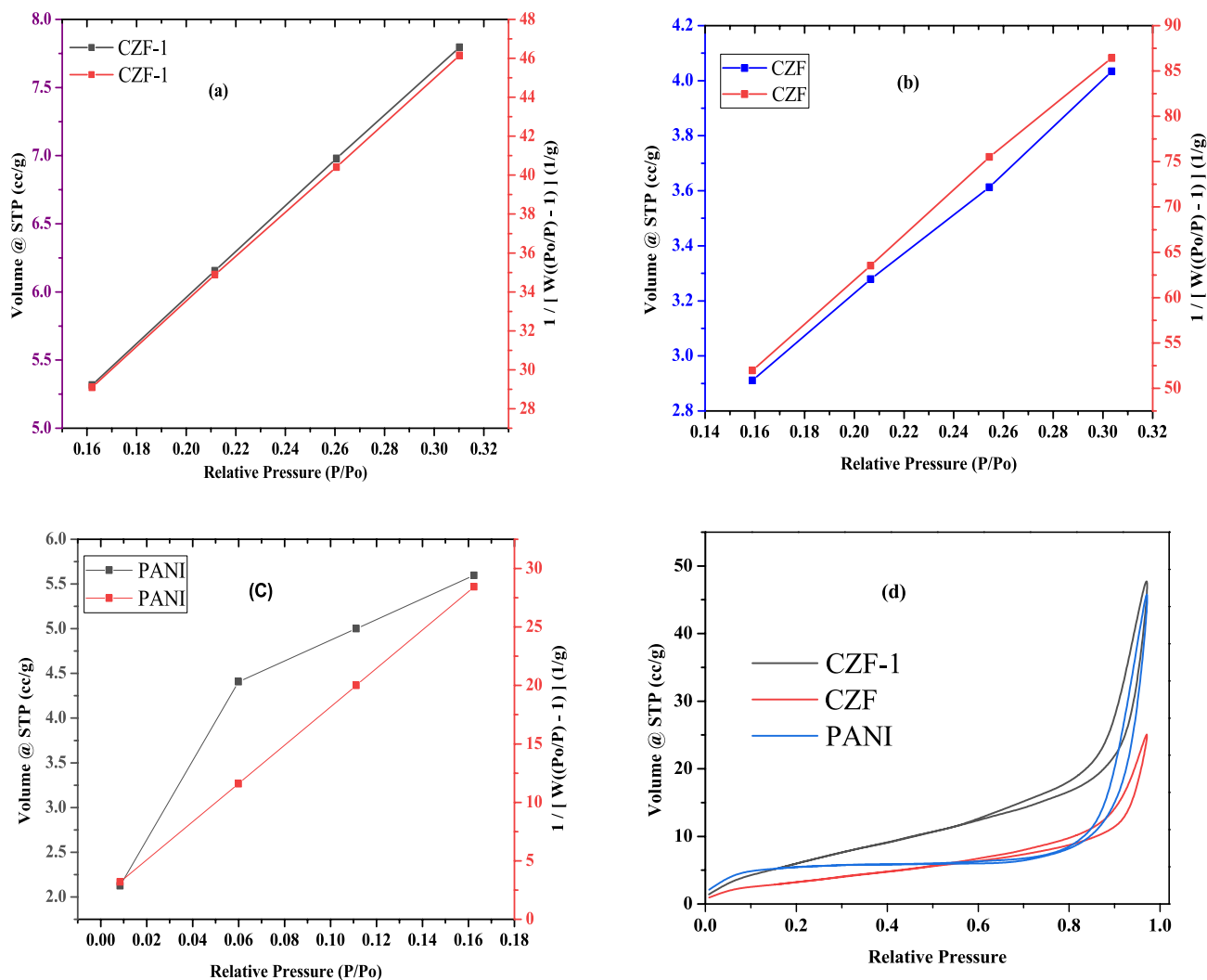
Fig. 7 **(a–c)** N_2 Adsorption isotherm of PANI, CZF and CZF-1 **d** Pore size of PANI, CZF, CZF-1 samples

nanocomposites, indicating the excellent purity. The EDX results and the X-ray diffraction (XRD) data were very well matched [41]. This change in elemental composition suggests that the PANI has successfully coated on the surface of the $Cu_{0.5}Zn_{0.5}Fe_2O_4$ nanoparticles, resulting in a hybrid nanocomposite material [42].

3.5 TEM analysis

TEM pictures of CZF and CZF-2 were captured in Fig. 10a and b. The computed crystallite sizes using Scherrer's equation were very well agreed with the crystallite sizes deduced from the XRD line broadening of the strongest (311) peak, which ranged from 40 to 45 nm [43, 44]. In the TEM images of CZF and

CZF-2 showed lattice fringes with interplanar spacings 'd' of 0.406 nm for (311) planes and 0.52 nm for (220) planes. The effective production of pure-phase polycrystalline cubic nanoparticles was confirmed by XRD and TEM studies. Figures 10a and b display the crystallite size histograms of CZF and CZF-2 nanocomposite samples. The PANI matrix equally distributes the spherically shaped CZF nanoparticles. For the CZF-2, the TEM images show particles with average sizes of 10–12 nm [45, 46]. The ex-suit process pounds the ferrite particles by attrition, resulting in a decrease in size. This includes grinding a combination of ferrite and PANI, which causes the particles to repeatedly collide with one another and reduces their size comparatively to CZF/PANI nanocomposite.
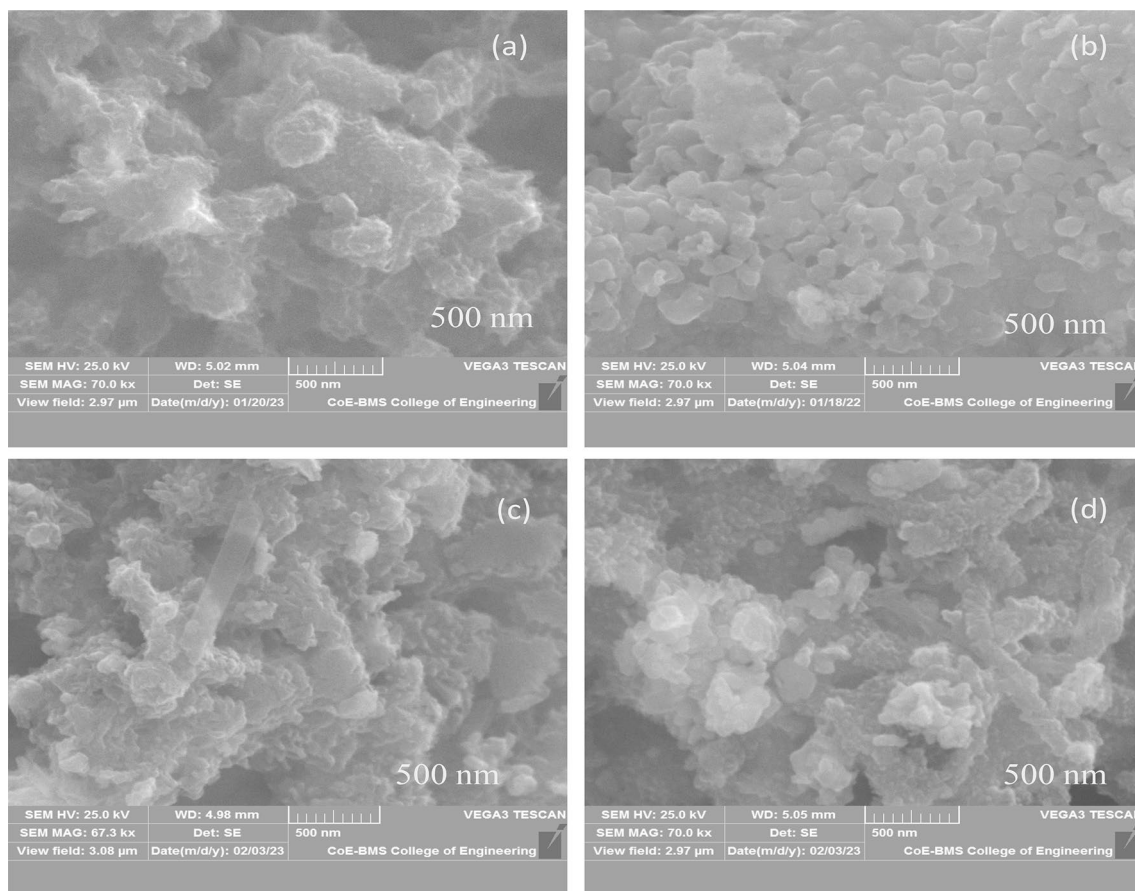
**Fig. 8** SEM images of **a** PANI **b** CZF **c** CZF-1 **d** CZF-2

3.6 VSM (vibrating-sample magnetometer)

Magnetization hysteresis loop tests at room temperature have been used to examine the specific magnetization property of PANI and PANI-CZF nanocomposites using a vibrating sample magnetometer (VSM) [47, 48]. PANI is the conducting polymer that may interact with CZF and other magnetic nanoparticles via charge transfer and other methods. Adding PANI can change the magnetic properties of the nanocomposite material by changing the magnetic anisotropy [47–49].

From Fig. 11, it was observed that the prepared nanocomposites show ferrimagnetic activity in the M-H loops. Table 3 shows the coercivity (Hc), remanent magnetization (Mr), and saturation magnetization of the PANI-CZF nanocomposites. It is abundantly obvious that when ferrite concentration increases, the values for magnetization (MS) rise. A significant observation was the enhancement of saturation magnetization (Ms) with increasing PANI content. The enhancement of the saturation magnetization (Ms)

with increasing PANI content can be attributed to the intrinsic magnetic moments of PANI. The interaction between PANI and the zinc-copper nano ferrite likely influenced the overall magnetic alignment, leading to a decrease in Ms. The reduced crystallite sizes can be attributed to the surface effects of the magnetic NPs. Surface spin disorders may lead to the formation of departed magnetic layers, providing a possible explanation for the reduced crystallite sizes. It is expected that when the size of the crystallites decreases, the number of spins at the surface of various produced ferrites will grow [49]. The higher magnetic interactions between the nanoparticles result in stronger magnetic coupling and a bigger saturation magnetization (Ms) value [49–51].

The magnetic moment and magnetic anisotropy of the nanoparticles may be reduced when the PANI concentration is increased in CZF nano ferrites because of the modifications made to the magnetic interactions and spin configurations. As a result, the magnetic saturation may be reduced and the coercivity of
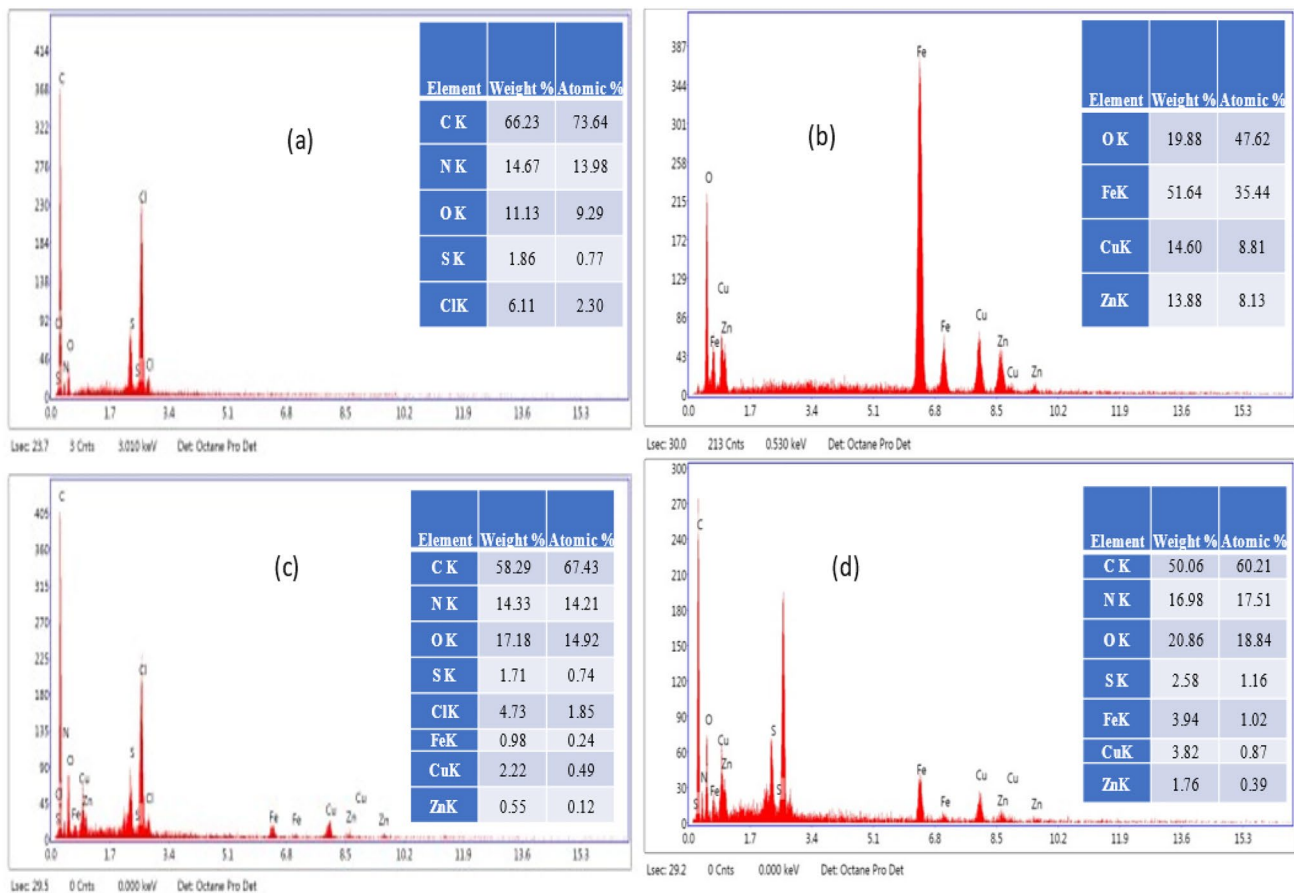
Fig. 9 EDAX spectra **a** PANI **b** CZF **c** CZF-1, **d** CZF-2

the nanocomposite material may rise. The crystalline structure, size, and number of the magnetic particles in the samples all affect the magnetic characteristics of composites containing magnetite or ferrite particles.

3.7 Dielectric properties

Figures 12 and 13 illustrate the real (ε') and imaginary (ε'') components of permittivity for the PANI, CZF, CZF-1, and CZF-2 nanocomposites. The addition of PANI to CZF results in an increase in their dielectric characteristics. Specifically, the incorporation of 30 wt% and 40 wt% of CZF resulted in a change in the dielectric constant, proving that PANI creates an interconnected network structure that alters the dielectric characteristics of the material. In Fig. 12, the trend of decreasing dielectric constant with increasing frequency indicates that the polarisation process in CZF is like a conducting phenomenon. The exchange of electrons between Fe^{2+} and Fe^{3+} e– causes local displacement of electrons in the direction of the applied electric field, which explains the polarisation of CZF [50, 52]. In Figs. 12 and 13, the complex dielectric constant is plotted against frequency, with high losses at low frequencies and low losses at higher frequencies [53, 54]. Defects and grain boundaries are attributed to the losses at low frequencies, while conducting grains are responsible for the losses at high frequencies [54]. For the CZF At low frequencies, the charge carriers' hopping frequency aligns with the externally applied electric field, leading to an increase in the dielectric constant. However, at higher frequencies, the charge carriers' hopping frequency cannot track the applied electric field, causing a reduction due to random dipolar orientation [55]. In CZF-1 and CZF-2 nanocomposites, the dielectric constant decreases with increasing frequency; the trend of the graph is the same for both real (ε') and imaginary (ε'') components of permittivity, but resonance occurs at a particular frequency. Interestingly, there is a sudden increase in the dielectric constant sharply with slight increases in frequency. A sharp peak is observed for
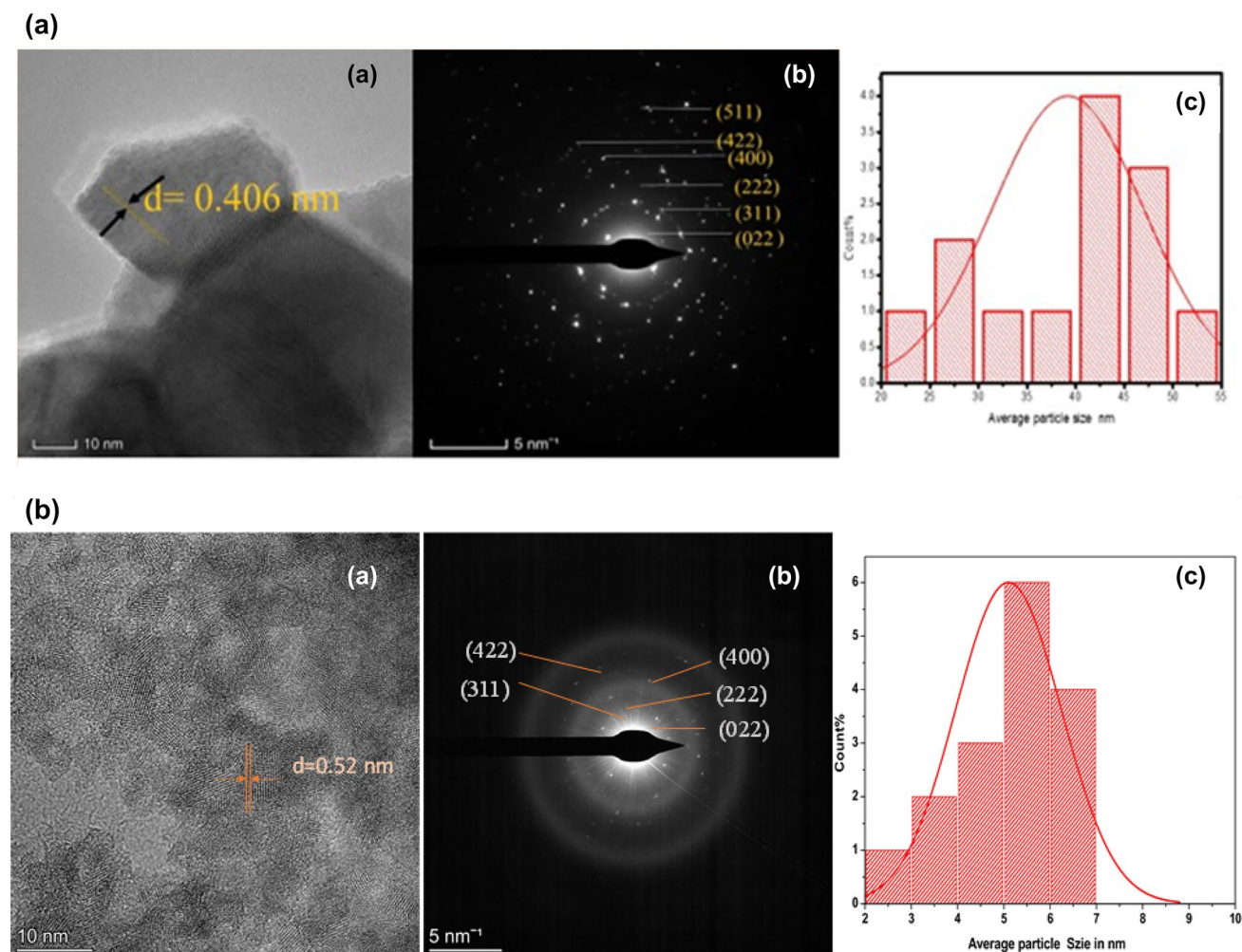
Fig. 10 a TEM images of CZF: (a) HR-TEM revealing lattice fringes of CZF, (b) The SAED pattern of CZF, and (c) displays a size histogram of CZF. **b** TEM images CZF-2: (a) HR-TEM revealing lattice fringes of CZF-2, (b) The SAED pattern of CZF-2, and (c) Displays a size histogram of CZF-2

the corresponding frequency, indicating a resonance behaviour [56, 57].

This behaviour is expected when the PANI-CZF nanocomposites samples are conductive, and skin effect becomes significant. At low-frequency regions, the resonance phenomenon for nanocomposites is mainly caused by vacancy or pores, provided that there exist space charges in the materials. At high-frequency regions, resonance behaviour is attributed to atomic and electronic polarization [56]. As the frequency increases, the dipoles in the individual materials begin to relax, causing the dielectric constant to decrease. Eventually, at higher frequencies, the interfacial polarization effect becomes negligible, and the dielectric constant returns to its original behaviour of constant with increasing frequency resulting

in a greater dielectric constant for the CZF-1 than the CZF-2 composite. The dispersion of the filler material in the matrix, as well as the frequency at which the dielectric constant was measured, [57] can all have an impact on the composite material dielectric constant.

3.8 AC conductivity

Figure 14 shows the room temperature frequency-dependent ac conductivity of pure polyaniline, CZF, CZF-1 and CZF-2 composites. The ac conductivity is almost constant at low frequencies, this is mainly due to very strong resistivity of the grain boundaries and causes a low conductivity [58]. For pure polyaniline conductivity obeys the universal power law, rising with higher frequencies [58]. Due to atomic
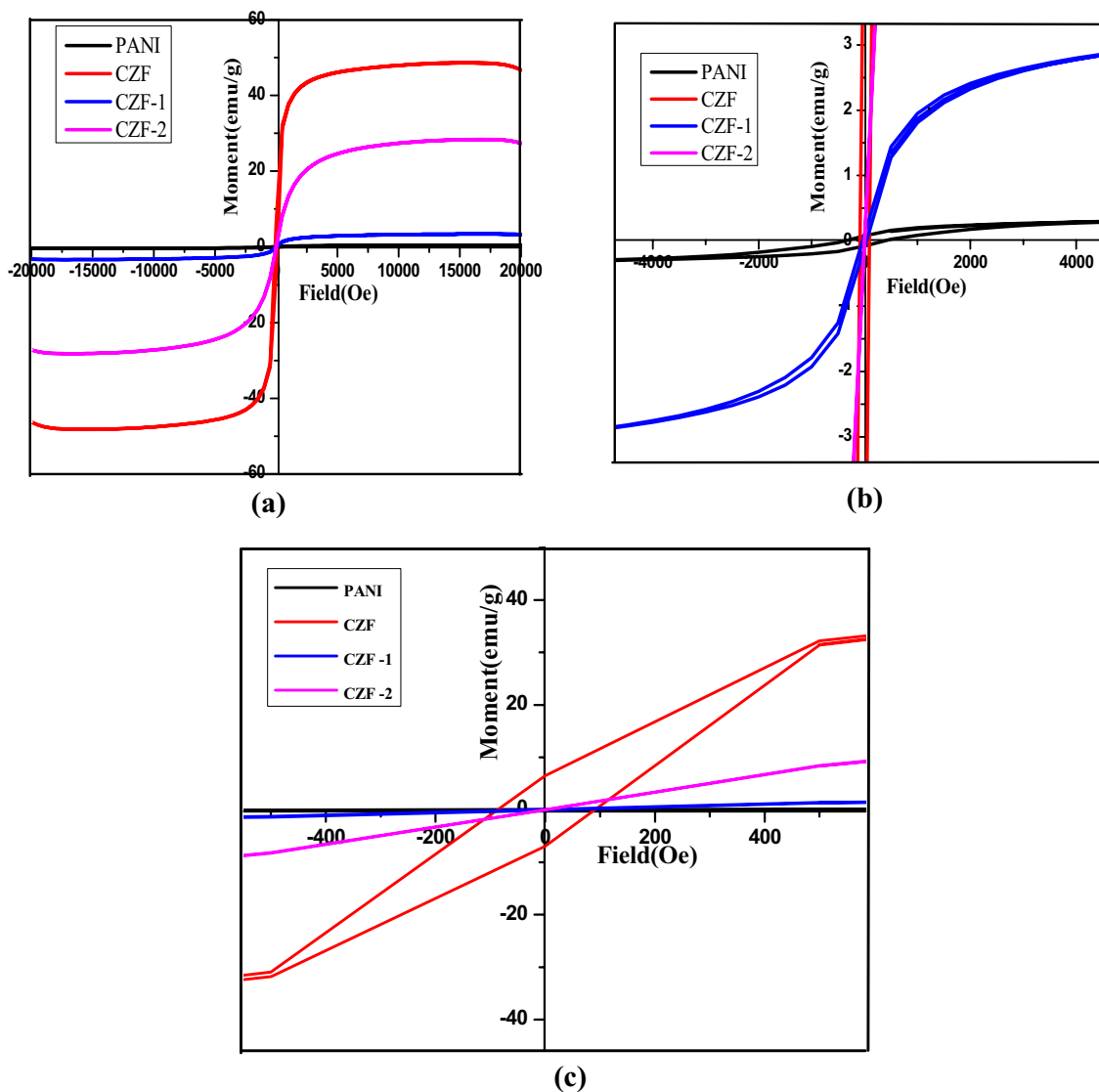
**Fig. 11 a** M-H loop PANI, CZF CZF-1, CZF-2 **b** and **c** are Zoom position of (a)

polarisation, CZF-1 composites exhibit conductivity of 0.0895 Scm^{-1} at 3.28 Hz and 0.1146 Scm^{-1} at 3.2 Hz. The conductivity of PANI-ferrite composite materials can

Table 3 The saturation magnetization (Ms), remnant magnetization (Mr), and coercivity (Hc) of CZF-PANI samples

Compounds	Coercivity (Hc) (Oe)	Remnant magnetization (Mr) emu/g	Saturation magnetization (Ms) emu/g
PANI	369	0.086	0.3
CZF	100	6.65	48.8
CZF-1	45	0.001	3.4
CZF-2	5	0.0006	28

be affected by various factors, including the relative concentrations of PANI and ferrite in the composite. At some specific frequencies, the charge carriers may be resonantly excited, or the relaxation of the charge carriers may occur. This can lead to a temporary increase in conductivity at those frequencies. However, at other frequencies, the charge carriers may not be resonantly excited, or the relaxation may not occur, leads to the sudden increase in conductivity at some frequencies and gradual decrease can be explained by the resonance or relaxation phenomena of the charge carriers [59] in the composite material.

The composition, synthesis method, concentration, stoichiometry, and particle size are a few of the
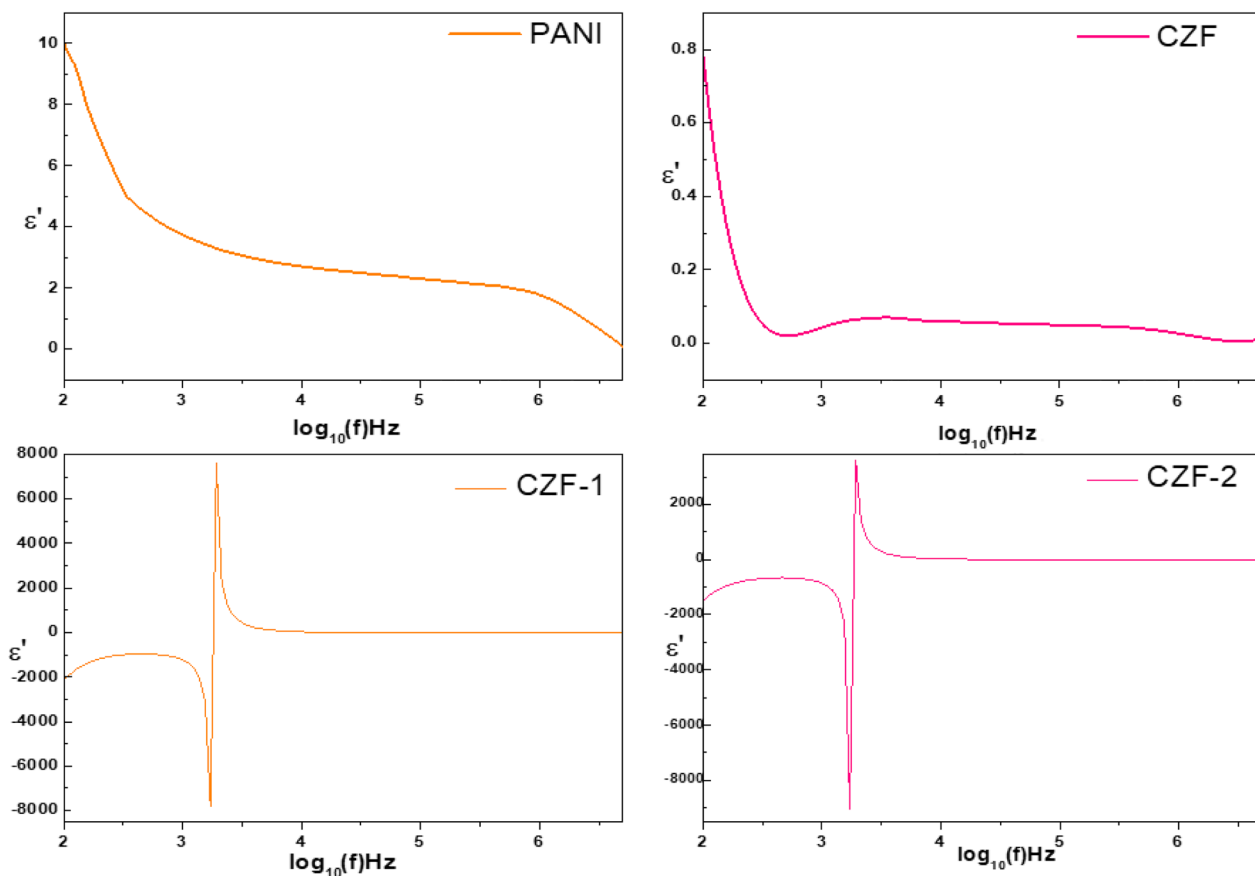
Fig. 12 Real dielectric constant of CZF, PANI, CZF-1, CZF-2 nanocomposites

variables that affect the dielectric loss tangent. The dielectric loss tangent is determined by taking the ratio of (ε'') and (ε') which is denoted as tanδ Eq. (2) [59, 60]

$$tan\delta = \frac{\varepsilon''}{\varepsilon'} \qquad (2)$$

The PANI and CZF frequency-dependent dielectric loss tangent (tanδ) plot is shown in Fig. 15. The dielectric loss tangent plot resembles the dielectric constant (ε') in appearance [61]. It was observed that the dielectric loss tangent (tanδ) is largest at low frequencies and minimum at higher frequencies [62].

In the case of PANI-ferrite, composites the addition of PANI to the ferrite nanoparticles results in a frequency-dependent dielectric loss tangent [63]. This means that the amount of energy that is dissipated in the material varies with the frequency of the applied electric field. The peak in the dielectric loss tangent plot at a frequency of 3.2 Hz is likely due to the resonance of the electric dipoles in the material at that frequency. This resonance can result in a large amount of energy being dissipated

in the material [64]. The combination of enhanced polarizability due to the addition of PANI, the magnetic properties of the ferrite nanoparticles likely contribute to the resonance [65] observed at 3.2 Hz in the dielectric loss tangent plot of the PANI-ferrite nanocomposites.

3.9 EMI shielding properties

Shielding effectiveness is the phenomenon of reducing the harmful electromagnetic radiation by using undesired interface between the source and receiver. EMI shielding is very important in industrial and military application. EMI shielding effectiveness (EMISE) was measured in dB. The three phenomena of reflection (SE_R), absorption (SE_A), and multiple reflection (S_M) are combined to form the electromagnetic interference shielding effectiveness (EMISE total), which is expressed as:

$$SE_T = SE_R + SE_A + SE_M \qquad (3)$$

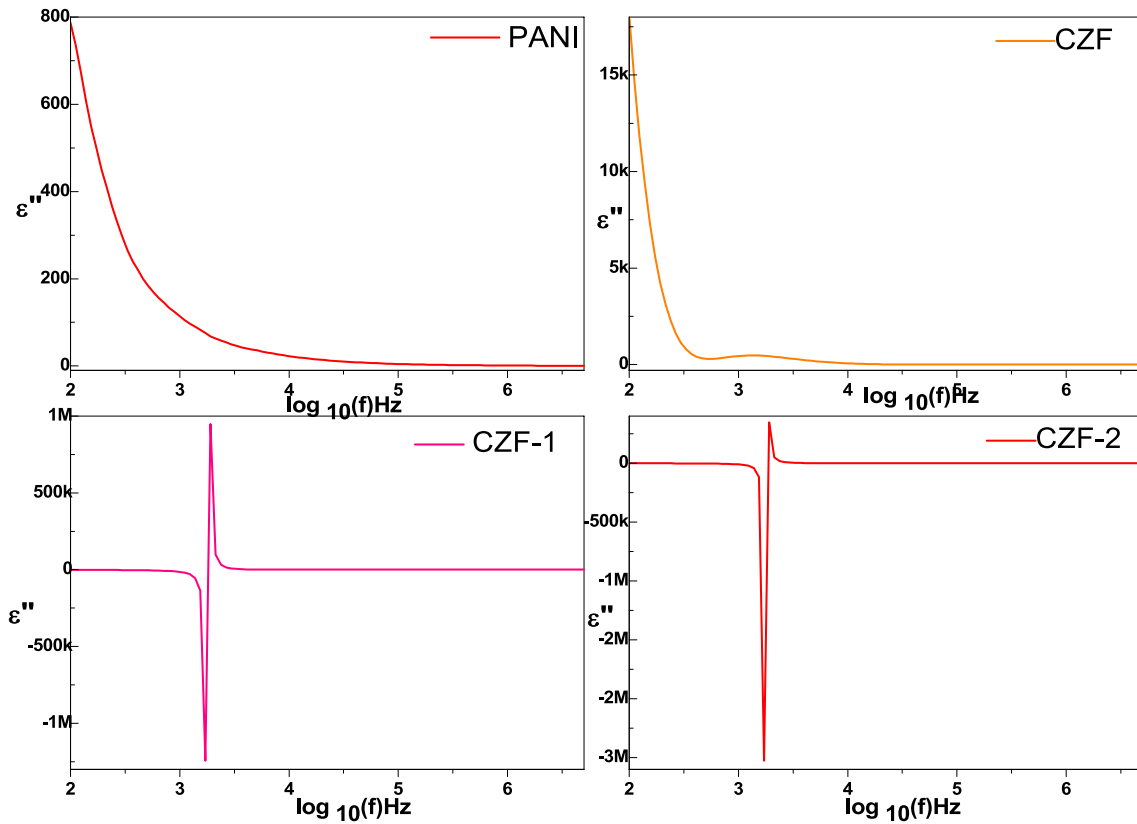The equations $SE_R = 10log_{10}(1 - R)$

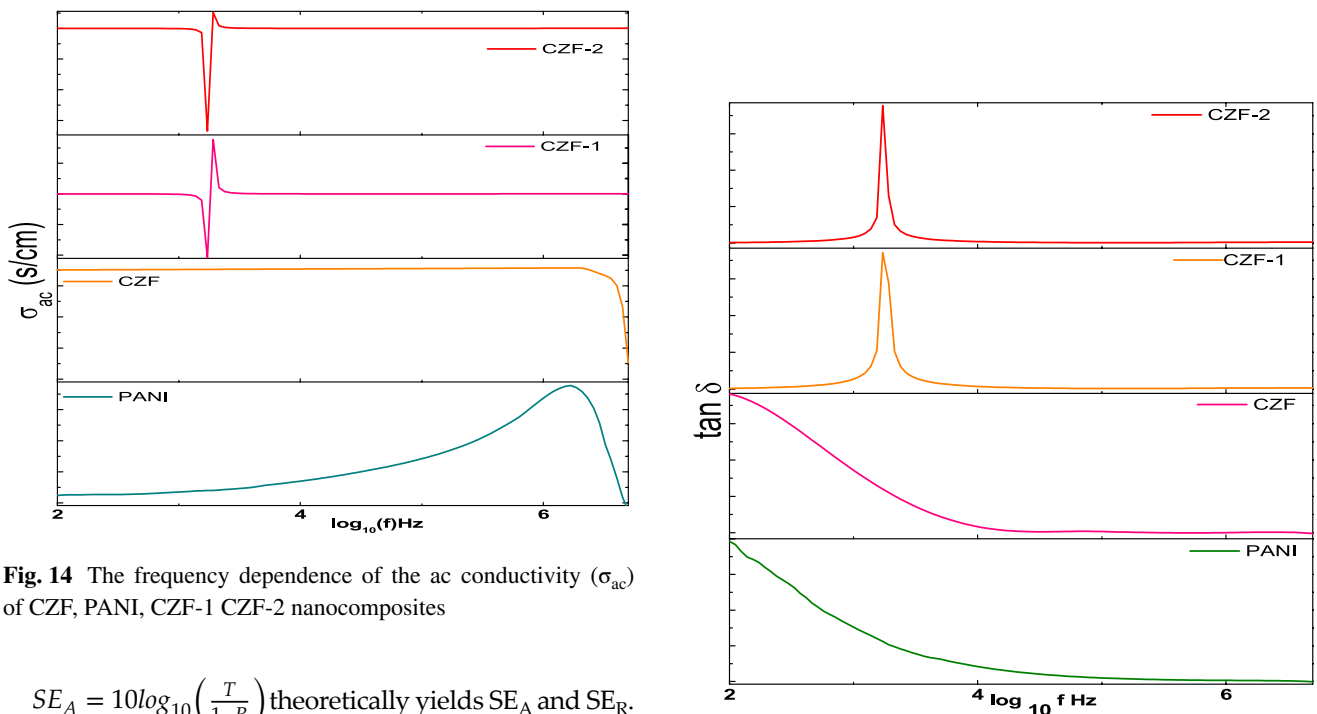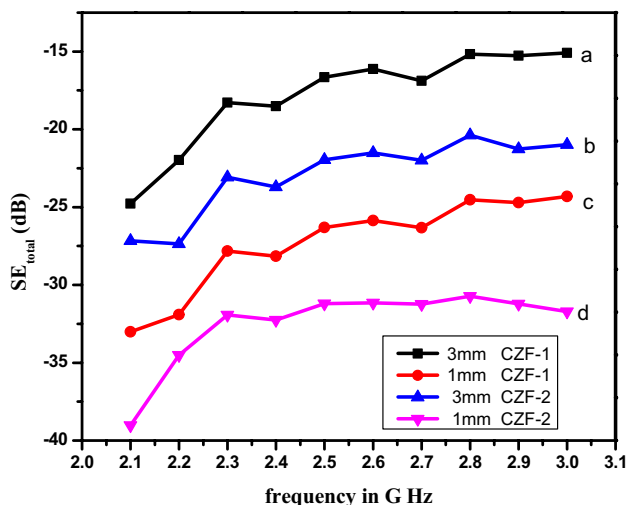**Fig. 13** Imaginary dielectric constant of CZF, PANI, CZF-1, CZF-2 nanocomposites

Fig. 14 The frequency dependence of the ac conductivity (σ_{ac}) of CZF, PANI, CZF-1 CZF-2 nanocomposites

$SE_A = 10log_{10}\left(\frac{T}{1-R}\right)$ theoretically yields SE_A and SE_R. Where the power coefficients of absorption (A),

Fig. 15 Tangent of dielectric loss (tanδ) of PANI, CZF, CZF-1, CZF-2 nanocomposites

Fig. 16 The total SE in dB with change in frequency of PANI-CZF nano composites, **a** 3 mm film of CZF-1, **b** 3 mm film of CZF-2, **c** 1 mm film of CZF -1, **d** 1 mm film of CZF -2

Table 4 EMI shielding effectiveness (dB) for different thickness CZF composites

PANI composite	Thickness of the film in mm	Frequency in G (Hz)	EMI shielding effectiveness. SE total (dB)
CZF-1	1	2.8	− 24
	3	2.8	− 15
CZF -2	1	2.8	− 32
	3	2.8	− 21

reflection (R), and transmission (T) are such that $A + R + T = 1$.

Total electromagnetic shielding effectiveness can be expressed as.

$$SE = -10log\left(\frac{P_T}{P_I}\right) = -20log\left(\frac{E_T}{E_I}\right) \qquad (4)$$

where P_I, (E_I) and P_T, (E_T) are the incident and transmitted powers of electromagnetic waves, respectively,

The fluctuation of the total EMI shielding effectiveness of PANI-CZF nanocomposite in the frequency range 2–3 GHz S-band is illustrated in the Fig. 16. From the Fig. 16, it was observed that, the shielding effectiveness increases with increases in the frequency of all the nano composites. According to experimental estimations shown in Table 4, the CZF-1 composite shows highest shielding effeteness as compared to CZF-2 nano composites. This is mainly due to high ac conductivity of the nanocomposite and magnetic property. The total shielding effective due to reflection is more as compared to total internal reflection and absorption. The 3 mm thickness CZF-1 and CZF-2 nanocomposite shows highest shielding effectiveness as compared to 1 mm thickness. Polymeric composites have multiple interfaces, each interface acts as effective EM radiation shielding at the surface. The electromagnetic shielding interference studies demonstrated significant effectiveness of CZF-1 nano composites at S-band frequencies. Comparative analysis against other materials reveals superior shielding effectiveness, attributed to the unique properties of CZF-1, making it a compelling choice for enhanced electromagnetic interference attenuation. The total shielding effectiveness increases with increase in thickness of the nanocomposite is mainly due to highest surface reflection, more absorption, and more time to interact with composite. As a result, these created composites may be employed successfully in EMI applications as microwave absorption materials. Table 5 shows the comparison of shielding effectiveness with similar type composites prepared by other investigators.

Table 5 Characteristics of Current Materials' Shielding Effectiveness in Comparison to Literature-Related Materials

Shielding material	Shielding performance(dB)	Thickness (mm)	Frequency region (G Hz)	Reference
$Zn_{0.5}Cu_{0.5}Fe_2O_4$/PANI	SE = 15	1	2–3	Present work
$Zn_{0.5}Cu_{0.5}Fe_2O_4$/PANI	SE = 24	3	2–3	Present work
$Mn_{0.5}Cu_{0.5}Fe_2O_4$/PANI	SE = 20			[66]
$Ni_{0.5}Cu_{0.5}Fe_2O_4$/PANI	RL = 39.6	2.5	7.5–13	[67]
$Mg_{0.6}Cu_{0.4}Fe_2O_4$/PANI	SE = 32.8		8–12	[68]

4 Conclusion

Using the Ex-suit method, successfully synthesized the PANI-CZF nanocomposites by incorporating PANI and CZF. CZF nanopowders were obtained through a green synthesis method known as solution combustion. For prepared samples XRD, SEM, BET, TEM, and EDAX analyses were performed to assess the structural characteristics of the nanocomposites. The FTIR confirms the characteristic bands of CZF nanoparticles at ~ 554 cm^{-1}, this was due to the presence of the structural vibrations in tetragonal metal-oxide (Zn^{2+}–O^{2-}, Fe^{3+}–O^{2-}) bonds & ~ 395 cm^{-1} was due to the presence of the structural vibrations of octahedral metal-oxide (Cu^{2+}–O^{2-}, Fe^{3+}–O^{2-}) bonds. BET analysis of CZF nanoparticles was performed it reveals the surface area of pores in the range 39.455 to 13.727 m^{2}g^{-1}. The PANI-CZF composite exhibited ferrimagnetic properties. These analyses confirmed the samples' purity, uniformity, and absence of any excess material. The addition of PANI to the zinc-copper nano ferrite significantly influenced its magnetic properties, enhancing saturation magnetization, reducing coercivity, and altering remanence, thereby opening avenues for tailored applications in magnetic devices. As the frequency increased, there was a slight decrease in the value of the dielectric constant. The real part of the permittivity displayed abrupt increases, while the imaginary part exhibited a sharp peak. The dielectric and magnetic properties of these nanocomposites contribute to the observed reflection loss. It was the combination of magnetic and conducting polyaniline that made it possible to get a shielding effectiveness of -15 dB in the S-band frequency range. Consequently, these nanocomposites hold great promise for applications in electromagnetic interference (EMI) shielding.

Author contributions

GH: conceptualization, methodology, investigations, writing original draft. DRR: data curation, writing original draft. RT: methodology, data Curation. CD: formal analysis, revieing and editing, validation, supervision. MR: conceptualization, formal analysis, methodology. MVM: data organization; characterization. KMR: conceptualization, formal analysis; methodology, supervision, writing–review & editing, visualization.

Data availability

Not Applicable.

Declarations

Conflict of interest The authors declare that they have no known competing financial interests or personal relationships that could have appeared to influence the work reported in this paper.

Ethical approval This article does not contain any studies with human participants or animals performed by any of the authors.

References

1. S. Sugimoto, K. Haga, T. Kagotani, K. Inomata, J. Magn. Magn. Mater. **1**, 1188 (2005)

2. P. Kallambadi Sadashivappa, R. Venkatachalam, R. Pothu, R. Boddula, P. Banerjee, R. Naik, A.B. Radwan, N. Al-Qahtani, J. Compos. Sci. **7**, 77 (2023)

3. D.A. David, M.J. Jabeen Fatima, A. Khan, R. Joy, V.K. Thakur, R.R. Ruiz-Rosas, S. Ozden, P. Raghavan, in *Handbook of porous carbon materials*. ed. by A.N. Grace, P. Sonar, P. Bhardwaj, A. Chakravorty (Springer, Singapore, 2023), pp.669–702

4. P. Angskog, P. Nasman, L.G. Mattsson, IEEE Trans. Electromagn. Compat. **61**, 1552 (2018)

5. Z. Wang, Z. Cheng, C. Fang, X. Hou, L. Xie, Mkagf sfksf khsfkshfk. Com. Part A App. Sci. Manuf. **136**, 105956 (2020)

6. D. Micheli, C. Apollo, R. Pastore, M. Marchetti, Comp. Sci. Tech **70**, 400 (2010)

7. P. Raju, P. Neelima, G.N. Rani, M. Kanakadurga, J. Phys. Chem. Solids **154**, 110048 (2021)

8. Shaik Jesus Mercy, D. Parajuli, N. Murali, A. Ramakrishna, Y. Ramakrishna, V. Veeraiah, K. Samatha, Appl. Phys. A **126**, 873 (2020)

9. M.S. Chavali, M.P. Nikolova, SN Appl. Sci. **1**(6), 607 (2019)

10. Santi Phumying, Sarawuth Labuayai, Chunpen Thomas, Vittaya Amornkitbamrung, Ekaphan Swatsitang, Santi Maensiri, Appl. Phys. A **111**, 1187 (2013)

11. Santi Phumying, Ekaphan Swatsitang SarawuthLabuayai, Vittaly Amornkitbamrung, S. Phumying. SantiMaensiri, Mater. Res. Bull. **48**, 2060 (2013)

12. A. Surjushe, R. Vasani, D.G. Saple, Indian J. Dermatol. **53**(4), 163–166 (2008)

13. S.P. Chandran, M. Chaudhary, R. Pasricha, A. Ahmad, M. Sastry, Biotechnol. Prog. **22**, 577 (2006)

14. S. Maensiri, P. Laokul, J. Klinkaewnarong, S. Phokha, V. Promarak, S. Seraphin, Opt. Adv. Mater. **2**(3), 161 (2008)

15. R. Gracia, D. Mecerreyes, Poly. Chem. **4**, 2206 (2013)

16. Y. Qiao, J. Xiao, Q. Jia, L. Lu, H. Fan, Results Phys **13**, 102221 (2019)

17. M.A. Almessiere, Y. Slimani, H.S. El Sayed, A. Baykal, J. Rare Earths **37**(7), 732–740 (2019)

18. Y. Slimani, B. Unal, M.A. Almessiere, E. Hannachi, G. Yasin, A. Baykal, I. Ercan, J. Mater. Sci.: Mater. Electr. **31**(10), 7786–7797 (2020)

19. A. Safeen, K. Safeen, M. Shafique, Y. Iqbal, N. Ahmed, M.A. Khan, G. Asghar, K. Althubeiti, S. Al Otaibi, G. Ali, W.H. Shah, RSC Adv. **12**(19), 1923–1932 (2022)

20. I. Jabbar, Y. Zaman, K. Althubeiti, S.A. Otaibi, M.Z. Ishaque, N. Rahman, M. Sohail, A. Khan, A. Ullah, T. Del Rosso, Q. Zaman, RSC Adv. **12**(21), 13456–13463 (2022)

21. M.P. Izaak, Y.E. Gunanto, H. Sitompul, Y. Sarwanto, W. Ari Adi, Key Eng. Mater. **940**, 31 (2023)

22. Zulfiqar, M. Zubair, A. Khan, T. Hua, N. Ilyas, S. Fashu, A.M. Afzal, M.A. Safeen, R. Khan, J. Mater. Sci.: Mater. Electron. **32**, 9463–9474 (2021)

23. R. Khan, V. Tirth, A. Ali, K. Irshad, N. Rahman, A. Algahtani, M. Sohail, S. Isalm, J. Mater. Sci.: Mater. Electr. **32**(16), 21631–21642 (2021)

24. M. Naagar, S. Chalia, P. Thakur, A. Thakur, *Emerging applications of low dimensional magnets*, 1st edn. (CRC Press, Baco Raton, 2023), pp.215–244

25. R. Khan, C.I. Levartoski. Zulfiqar, T. de Araujo, A. Khan, B. Khan, S. Fashu. Ullah, J. Mater. Sci.: Mater. Electr. **29**, 9785–95 (2018)

26. R. Khan, K. Althubeiti, A.M. Zulfiqar, N. Afzal, S. Rahman, W. Fashu, A. Zhang, R. Zheng. Khan, J. Mater. Sci.: Mater. Electr. **32**, 24394–24400 (2021)

27. B.J. Madhu, M. Gurusiddesh, T. Kiran, B. Shruthi, H.S. Jayanna, J. Mater. Sci. Mater. Electron. **27**, 7760 (2016)

28. Y. Salem, B. Unal, M.A. Almessiere, E. Hannachi, G. Yasin, A. Baykal, I. Ercan, J. Mater. Sci.: Mater. Electr. **31**(10), 7786–7797 (2020)

29. A. Hamrita, Y. Slimani, M.B. Salem, E. Hannachi, L. Bessais, F.B. Azzouz, M.B. Salem, Ceram. Int. **40**(1), 1461–1470 (2014)

30. A.H. Elsayed, M.M. Eldin, A.M. Elsyed, A.A. Elazm, E.M. Younes, H.A. Motaweh, Int. J. Electrochem. Sci. **6**(1), 206 (2011)

31. M.A. Almessiere, Y. Slimani, H. Güngüneş, S. Ali, A. Manikandan, I. Ercan, A. Baykal, A.V. Trukhanov, Nanomaterials **9**(6), 820 (2019)

32. M.A. Almessiere, Y. Slimani, M. Sertkol, M. Nawaz, A. Sadaqat, A. Baykal, I. Ercan, B. Ozçelik, Nanomaterials **9**(3), 430 (2019)

33. R. Mashuri, M.A. Baqiya, R. Triwikantoro, E. Yahya, R. Darminto, AIP Conf. Proc. **1415**, 238 (2011)

34. M. Zeshan, M.S. Waheed, S.A. Ishaq, A. Siddique, A. Ullah, E.S. Sherif, M.Z. Ansari, S.A. Khan, A.R. Khan, H.M. Farid, Chem. Pap. **77**(11), 6533–6542 (2023)

35. S. Taneja, D. Chahar, P. Thakur, A. Thakur, J. Alloys Compd. **859**, 157760 (2021)

36. L. Munteanu, A. Munteanu, M. Sedlacik, E. Kutalkova, M. Kohl, A. Kalendova, J. Ind. Eng. Chem. **115**, 440 (2022)

37. R. Thejas, G.D. Prasanna, G. Nagaraju, M.V. Murugendrappa, C.S. Naveen, Proc. Inst. Mech. Eng. Part E: J. Process Mech. Eng. **237**(2), 162 (2023)

38. M. Hashim, S.E. Shirsath, S.S. Meena, R.K. Kotnala, S. Kumar, P. Bhatt, R.B. Jotania, R. Kumar, Mater. Chem. Phys. **141**(1), 406–415 (2013)

39. Saad Hassan, Ayman H. Kamel, Amr A. Hassan, Abd Amr, Heba Abd El-Naby, Mohamed Al-Omar, Ahmed Sayed, Molecules **25**(12), 2721 (2020)

40. S. Kotresh, A. Roy, A. Parveen, N. Badi, A. Murali, J. Mater. Sci.: Mater. Electron. **34**(3), 218 (2023)

41. P. Raju, P. Neelima, G.N. Rani, M. Kanakadurga, J. Phys. Chem. Solids **154**, 110048 (2021)

42. G.D. Prasanna, H.S. Jayanna, V. Prasad, J. Appl. Polym. Sci. **120**(5), 2856–2862 (2011)

43. N. Hwang, A.R. Barron, The connexions project. pp. 1–1 (2011)

44. N. Ikramullah, F. Ali, Z.A. Ali, M. Sheikh, I. Bilal, Ahmad. Water Air Soil Pollut. **231**, 1–2 (2020)

45. A. Maleki, Z. Hajizadeh, P. Salehi, Sci. Rep. **9**(1), 5552 (2019)

46. P. Jing, J. Li, L. Pan, J. Wang, X. Sun, Q. Liu, J. Hazard. Mater. **284**, 163–70 (2015)

47. S. Kotresh, A. Roy, A. Parveen, N. Badi, A. Murali, J. Mater. Sci. Mater. Electron. **34**(3), 218 (2023)

48. H. Sozeri, U. Kurtan, R. Topkaya, A. Baykal, M.S. Toprak, Ceram. Int. **39**(5), 5137 (2013)

49. G. Vishnu Priya, N. Murali, M.K. Raju, D. Bal Krishan, Praveen Choppara Parajuli, B. Chandra Sekhar, Ritesh Verma, Khalid Mujasam Batoo, P.V. Lakshmi Narayana, Appl. Phys. A **128**, 663 (2022)

50. Z.A. Al-Hasnawy, K.K. Jasim, M.A. Awad, HIV Nurs. **23**(1), 463 (2023)

51. M. Majhi, R.B. Choudhary, P. Maji, Bull. Mat. Sci. **38**, 1195 (2015)

52. J. Su, Q. Ma, L. Que, H. Jiang, X. Xu, Y. Wang, Y. Guo, Z. Zhou, Nano Res. **16**, 6369 (2023)

53. P. Paulraj, A. Umar, K. Rajendran, A. Manikandan, R. Kumar, E. Manikandan, K. Pandian, M.H. Mahnashi, M.A. Alsaiari, A.A. Ibrahim, N. Bouropoulos, Electrochim. Acta **363**, 137158 (2020)

54. A.S. Hameed, H. Bahiraei, M.V. Reddy, M.Z. Shoushtari, J.J. Vittal, C.K. Ong, B.V. Chowdari, ACS Appl. Mater. Interfaces **6**(13), 10744 (2014)

55. A. Choudhury, Sens. Actuators B Chem. **138**(1), 318 (2009)

56. M. Khairy, J. Alloys Compd. **608**, 283 (2014)

57. B. Trinadh, J. Suresh, A. Rama Krishna, K. Vijaya Babu, B. Vikram Babu, P.V.S.S.S.N. Reddy, B. Sathish Mohan, K. Samatha, Appl. Phys. A **129**, 48 (2023)

58. M. Zeshan, M. Ali, M.M. Alanazi, S.M. Abdelmohsen, R.Y. Khosa, A.G. Al-Sehemi, M.Z. Ansari, R.A. Tayeb, H.M.T. Farid, M.M. Rahman, Ceram. Int. **49**, 20536 (2023)

59. M.A. Almessiere, Y. Slimani, A.D. Korkmaz, A. Baykal, H. Güngüneş, H. Sözeri, S.E. Shirsath, S. Güner, S. Akhtar, A. Manikandan, RSC Adv. **9**(53), 30671–30684 (2019)

60. S. Kour, S.K. Adhikari, M. Palihawadana, R. Mukherjee, J. Inorg. Organomet. Polym. **33**, 1704 (2023)

61. A.M. Henaish, M.M. Ali, D.E. Refaay, I.A. Weinstein, O.M. Hemeda, J. Inorg. Organomet. Polym. **31**, 731 (2021)

62. A. Manikandan, J.J. Vijaya, L.J. Kennedy, M. Bououdina, J. Mol. Struct. **1035**, 332 (2013)

63. E.E. Tanrıverdi, A.T. Uzumcu, H. Kavas, A. Demir, A. Baykal, Nano-Micro Lett. **3**, 99 (2011)

64. M.B. Mohamed, E.S. Karimat, Compos. B Eng. **56**, 270 (2014)

65. R.S. Priya, P. Chaudhary, E.R. Kumar, A. Balamurugan, C. Srinivas, G. Prasad, M. Deepty, V. Praveenkumar, B.C. Yadav, D.L. Sastry, Y. Al-Douri, Ceram. Int. **48**(11), 15243 (2022)

66. S.A. Ansari, A. Nisar, B. Fatma, W. Khan, A.H. Naqvi, Mat. Sci. Eng. B **177**(5), 428 (2012)

67. Y. Slimani, B. Unal, M.A. Almessiere, A.D. Korkmaz, S.E. Shirsath, G. Yasin, A.V. Trukhanov, A. Baykal, Res. Phys. **17**, 103061 (2020)

68. O. Yalçın, H. Bayrakdar, S. Ozum, J. Magn. Magn. Mater. **343**, 157 (2013)